ADVANCED OPTICAL MATERIALS
www.advopticalmat.de

Simultaneous Determination of Transition Dipole Moment Orientation and Refractive Index in Morphologically Non-Uniform Nanoscale Films

Donghyeon Shin, Seungyeon Cho, Jaehyun Lee, Kyusung Choi, Jinwon Jun, Min-Gon Shin, Dong Jin Shin, Seokho Kim, Jae-Min Myoung, Jun Yeob Lee, Jaesang Lee, Namyoung Ahn, Kyusang Lee,* and Jongchan Kim**

A high-precision, single-shot technique simultaneously quantifies the refractive index and transition dipole moment orientation in nanoscale emissive films using Fourier imaging microscopy. Direct capture of momentum-space (*k*-space) emission patterns in a polarization-resolved setup enables characterization of anisotropic optical properties. This approach overcomes limitations of conventional ellipsometry and angle-dependent photoluminescence measurements, which typically require predefined refractive index models and atomically smooth interfaces. The method determines anisotropic refractive indices and in-plane transition dipole moment orientations across various emissive systems, including organic films, quasi-2D perovskite layers, and quantum dot layers, even in the presence of nanoscale morphological disorder. The experimental result yields parameters with a precision of within 1% and 0.01 for transition dipole moment orientation and refractive index, respectively. The measured refractive index shows good agreement with conventional ellipsometry measurements. The extracted parameters strongly correlate with enhancements in optical outcoupling efficiency. These findings highlight the utility of Fourier imaging microscopy as a diagnostic tool for designing and optimizing next-generation optoelectronic devices.

1. Introduction

Fourier Image Microscopy (FIM) has emerged as a powerful tool for determining the transition dipole moment (TDM) orientation by capturing angle-resolved emission patterns in single-shot measurements, eliminating the need for sample rotation while enabling rapid measurements with minimized alignment errors.[1–20] However, current analyses rely on predefined refractive indices at emission wavelength, introducing substantial inaccuracies when assumed values deviate from the actual values.[3,5,10,21–23] For instance, Kim et al.[10] demonstrated that neglecting refractive index anisotropy in some organic materials led to noticeable deviations in TDM orientation results. Similarly, Ekhoff et al.[24] showed that polarization-resolved measurements are sensitive to such inaccuracies. Moreover, extracting an accurate refractive index, particularly for the extraordinary component in thin organic films, remains challenging. Conventional ellipsometry primarily probes in-plane optical properties and lacks the path needed to resolve out-of-plane anisotropy. Its accuracy further degrades in the presence of surface roughness, which disrupts the interference between reflected light from the film interfaces.

In this work, we present a universal method based on FIM that simultaneously determines the refractive indices and TDM

D. Shin, S. Cho, K. Choi, M.-G. Shin, N. Ahn, J. Kim
Department of Integrated Display Engineering
Yonsei University
50 Yonsei-ro, Seodaemun-gu, Seoul 03722, Republic of Korea
E-mail: n.ahn@yonsei.ac.kr; jck@yonsei.ac.kr

J. Lee, J. Jun, J. Lee
Department of Electrical and Computer Engineering
Seoul National University
Seoul 08826, Republic of Korea

D. J. Shin, J. Y. Lee
School of Chemical Engineering
Sungkyunkwan University
2066, Seobu-ro, Jangan-gu, Suwon-si, Gyeonggi-do 16419, Republic of Korea

The ORCID identification number(s) for the author(s) of this article can be found under https://doi.org/10.1002/adom.202502019

DOI: 10.1002/adom.202502019

S. Kim, K. Lee
Department of Electrical and Computer Engineering
University of Virginia
Charlottesville, VA 22904, USA
E-mail: kl6ut@virginia.edu

J.-M. Myoung
Department of Material Science and Engineering
Yonsei University
50 Yonsei-ro, Seodaemun-gu, Seoul 03722, Republic of Korea

K. Lee
Department of Materials Science and Engineering
University of Virginia
Charlottesville, VA 22904, USA

J. Kim
School of Electrical and Electronic Engineering
Yonsei University
50 Yonsei-ro, Seodaemun-gu, Seoul 03722, Republic of Korea

orientation without requiring prior optical constants. The approach employs direct fitting of measured polarization-dependent *k*-space polar plots to extract both parameters. Ordinary refractive indices are obtained from s-polarized emission patterns (sPP), which then serve as inputs for extracting extraordinary refractive indices and TDM orientations from p-polarized patterns (pPP). This approach remains robust even for films with rough nanostructures such as polycrystalline perovskite materials or quantum dot (QD) films. By enabling precise optical characterization in complex morphologies, our method shows potential to advance the optical design of next-generation optoelectronic devices.

2. Results and Discussion

2.1. Angular Emission Analysis Using Fourier Imaging Microscopy

The angular distribution of emissions from organic thin films is governed by three fundamental factors: the thickness of the thin film, orientation of transition dipole moments (TDMs), and the refractive index of the material. In this study, Fourier imaging microscopy (FIM) is employed to simultaneously extract the TDM orientation and refractive index, enabling a comprehensive understanding of the optical behavior of thin films.

The experimental setup of FIM is illustrated in **Figure** 1a. It comprises an inverted photoluminescence microscope with a laser for optically pumping the sample. Emitted photoluminescence (PL) of the sample is captured by the objective lens, which maps the 3D angular distribution of the emitted light into a 2D polar plot profile with respect to the in-plane wavevectors, $k_{||}$, in the Fourier plane. As illustrated in Figure 1b, the region bounded by $0 < k_{||} / k_0 < 1$ indicates the air mode, representing the amount of light extracted toward the air within the escape cone. The region $1 < k_{||} / k_0 < n_{glass}$ ($n_{glass} \approx 1.5$) shows the signal of the substrate mode. It contains both lights emitted toward the glass substrate and those initially emitted toward the air (red arrows) but redirected into the substrate by total internal reflection (blue arrows) as shown in the schematic illustration on the left-hand side of Figure 1b. The light coupled into the substrate mode is collected via index-matched oil with the refractive index identical to the glass substrate which removes the total internal reflection at the air-glass interface. The right-hand side of Figure 1b is a schematic showing a Fourier transform of the photoluminescence of the light source that converts real space image to a momentum space that results in a polar plot which corresponds to the angular emission profile of the light source.

Figure 1c illustrates how a linear polarizer separates the emitted light into s- and p-polarized components, forming the s- and p-polarized plane (sPP and pPP), respectively.1 The emission from sPP arises from horizontally aligned TDM respect to the substrate plane (pPP_{hor}) that is perpendicular to the plane of incidence. In contrast, the pPP contains contributions from both horizontally (pPP_{hor}) and a vertically oriented TDMs (pPP_{ver}) respect to the substrate plane, as it probes electric field components parallel to the incidence plane. The angular intensity distribution of the pPP is thus sensitive to the relative contributions of these two orthogonal TDM components. The TDM orientation is quantified by the horizontal dipole ratio denoted as θ_{hor}, which ranges from 0 (fully vertical) to 1 (fully horizontal), with a value of 0.67 corresponding to an isotropic distribution of TDMs.

2.2. Parameter-Dependent Variations in *k*-Space Emission Intensity Distributions

Figure 2 presents the calculation results illustrating the influence of refractive index and θ_{hor} on sPP and pPP of the polar plot intensity spectrum. These spectra show the relative intensity at varied parallel *k* vectors normalized to the value at $k_{||} = 0$, with the spectra on sPP in the region of $k_{||}/k_0 < 0$ and pPP in $k_{||}/k_0 > 0$ where k_0 is the free space wavevector. Since both the refractive index and TDM orientation affect the intensity spectrum, they are utilized to determine the refractive index as well as the orientation of the TDM.

In Figure 2a, influence of the film refractive index in sPP and pPP was investigated. As the refractive index increases from 1.6 to 3.0, the relative intensity at $k_{||}/k_0 = -1.1$ on sPP decreases by 63%, while the relative intensity at $k_{||}/k_0 = 1.1$ on pPP decreases by 77%. This reveals that the refractive index of the emissive layer influences the angular emission pattern, even in films as thin as 30 nm. The dependence arises from Fresnel reflection at various angles at both the EML-air and EML-glass interfaces. As *n* increases, the index contrast and thus reflectivity become more pronounced, especially near and beyond the critical angle, $k_{||} \ /k_0 \ \approx n_{\mathrm{glass}}$ and in the region of $k_{||}/k_0 > 1$. These trends provide a non-invasive route to extract *n* through direct comparison with experimental FIM results. (see Figure S1, Supporting Information)

In contrast, Figure 2b illustrates the variation of intensity spectra on sPP and pPP with changes in θ_{hor} with fixed refractive index and film thickness. The intensity spectrum in sPP shows no change with θ_{hor}, while it decreases on pPP causing the relative peak intensity at $k_{||}/k_0 = 1.1$ to reduce significantly, by 99.9%. This behavior reflects the polarization selectivity of dipole coupling: vertically oriented TDMs couple efficiently to high-*k* modes such as glass and waveguide modes on the pPP, which possess a strong out-of-plane electric field component. In contrast, horizontal dipoles emit weakly into these high-*k* modes and rather emit strongly into the air modes. This sensitive response of pPP intensity spectra depending on θ_{hor}, combined with the stability of sPP, allows determination of TDM orientation using pPP spectra, while sPP being used to probe the film refractive index.

Figure 2c,d demonstrates the impact of birefringence, dissecting the role of ordinary (n_{o}) and extraordinary refractive indices (n_{e}) on the *k*-space emission pattern with constant θ_{hor} and thickness. The emission pattern strongly depends on the refractive index in the direction of the TDM oscillation.

Figure 2c illustrates how variations in the n_{o} affect both sPP and pPP emission patterns. The relative intensity at $k_{||}/k_0 = -1.1$ on sPP decreases by 38% as n_{o} increases from 1.6 to 2.5, while the relative intensity at $k_{||}/k_0 = 1.1$ on pPP decreases by 53%. Notably, the sPP pattern undergoes a global transformation, which arises from the fact that the TDM responsible for sPP is oriented perpendicular to the plane of incidence, causing the TDM to be parallel to the ordinary optical axis. Consequently, according to the Maxwell boundary conditions, n_{o} governs the optical response for all in-plane wavevectors ($k_{||}$), thereby

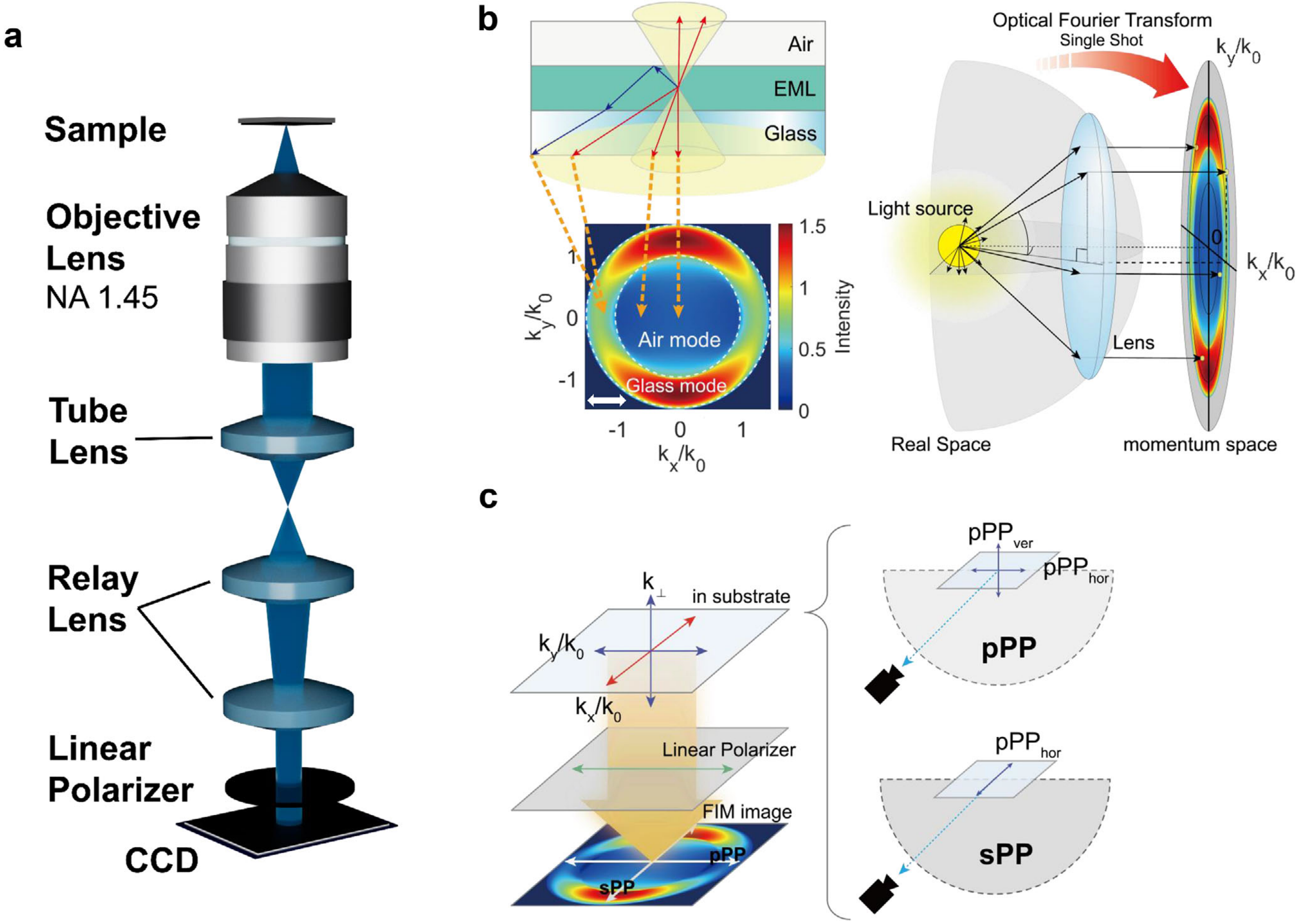

Figure 1. a) Diagram of the Fourier plane imaging microscope measurement system. b) A schematic illustration showing how light from the emissive layer (EML) couples into the distinct light modes. Each mode, air mode ($k_{||}/k_0 < 1$) and glass mode ($1 < k_{||}/k_0 < 1.5$), are indicated in the *k*-space pole plot. The red arrows designate light that directly propagates to air or glass, while the blue arrows represent light that is reflected at the EML-air interface and subsequently enters the glass mode in *k*-space. In the right-hand side, a 3-dimensional schematic shows how a lens transforms the real space image of the emitted light from the light source into momentum space. c) Schematic illustration showing the relationship between the coordinate system and polarization-resolved measurements, demonstrating how linear polarizer (green arrow) selectively filters each TDM component in sPP and pPP configurations. The filtered out TDM vector by the linear polarizer is shown with a red arrow.

influencing the entire sPP pattern. In contrast, the pPP pattern originates from TDMs lying within the incident plane, resulting in an electric field that possesses both in-plane (ordinary) and out-of-plane (extraordinary) dipoles respect to the substrate plane. When $k_{||}/k_0$ is close to zero, the electric field is predominantly aligned with the in-plane direction, and thus the emission is primarily determined by n_o. As $k_{||}/k_0$ increases, the out-of-plane component becomes more prominent, enhancing the influence of the n_e. Consequently, changes in n_o mainly affect the region $k_{||}/k_0 < 1$ in the pPP pattern. The major variation in Figure 2c pPP mainly occurs in the region of $k_{||}/k_0 > 1$ due to the normalization at $k_{||}/k_0 = 0$, which reverses the actual trend shown in Figure S2 (Supporting Information).

Figure 2d illustrates how variations in the n_e modulate the sPP and pPP patterns. As n_e increases from 1.6 to 2.5, the relative intensity on sPP remains constant, while the highest intensity peak on pPP increases by 48%. As previously discussed, the sPP pattern remains insensitive to n_e since the TDM orientation is perpendicular to the incident plane and thus orthogonal to the extraordinary optical axis. In contrast, the pPP becomes increasingly sensitive to n_e in the region $k_{||}/k_0 > 1$, where the electric field component aligned with the extraordinary axis is maximized. As a result, tuning n_e leads to pronounced modifications in the high-*k* region ($k_{||}/k_0 > 1$) of the pPP pattern.

The results in Figure 2 demonstrate that variations in refractive indices (n_o, n_e), TDM orientation (θ_{hor}), and optical anisotropy induce distinct and quantifiable changes in the calculated sPP and pPP spectra, each governed by a different physical mechanism. As noted, n_o governs the overall response of sPP by determining the in-plane electric field interaction, n_e reshapes the spectral profile of pPP in the high-*k* region through its control of the out-of-plane field component, and θ_{hor} modulates the coupling efficiency of TDMs to either air modes or high-*k* modes, thereby regulating the overall pPP intensity. Because these spectral signatures respond uniquely to each parameter, n_o can be determined by comparing the measured sPP emission pattern with the corresponding calculated result, while n_e and θ_{hor} can be determined by comparing the measured pPP pattern with

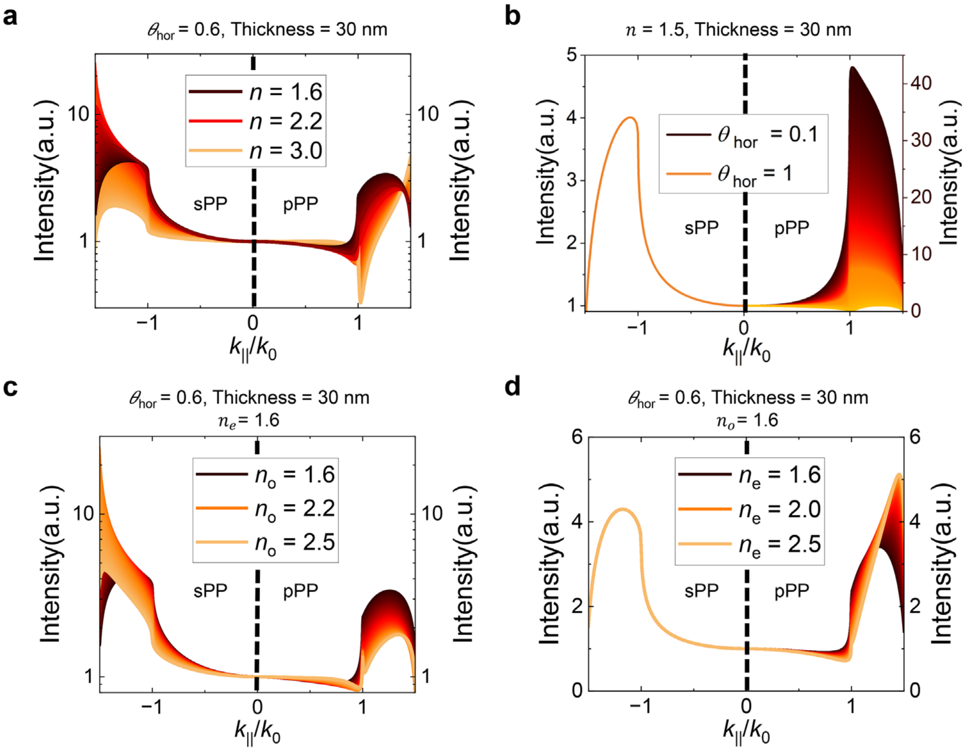

Figure 2. a) Calculated k-space intensity distributions on sPP ($k_{||}/k_0 < 0$) and pPP ($k_{||}/k_0 > 0$) for varying refractive indices ($n = 1.6$–3.0) with fixed $\theta_{hor} = 0.6$ and thickness = 30 nm. (b) Calculated intensity distributions for varying TDM orientations ($\theta_{hor} = 0.1$–1.0) with fixed refractive index $n = 1.5$ and thickness = 30 nm. c) Calculated intensity distributions for varying ordinary refractive indices (n_o = 1.6-2.5) with fixed $\theta_{hor} = 0.66$ and thickness = 30 nm. d) Calculated intensity distributions for varying extraordinary refractive indices (n_e = 1.6–0.5) with fixed $\theta_{hor} = 0.66$ and thickness = 30 nm. All intensity distributions are normalized to the value at $k_{||}/k_0 = 0$.

simulation. This procedure enables the determination of both the TDM orientation and the film refractive indices.

2.3. Transition Dipole Moment Orientation of Perovskite Nanocrystals

Figure 3 shows the correlation between the structural and optical properties of a 45nm-thick Phenethyl ammonium bromide (PEABr)–CsPbBr quasi-2D organic halide perovskite film, investigated by the measured and calculated Fourier plane images. Figure 3a shows a schematic illustration of the quasi-2D organic halide perovskite film. PEABr and CsPbBr are mixed at 1:1 mole ratio to maximize the formation of quasi-2D perovskite crystals. Cross-sectionally, the as-prepared film forms a stacked heterostructure with sublayers assigned to $N = 2$, $N = 3$, and 3D-like (bulk). Consistent with inter-sublayer energy transfer from thinner to thicker wells, the steady-state PL exhibits three resolved features. Accordingly, the PL in Figure 3b is modeled with Gaussian peaks for $N = 2$ and $N = 3$ and a double-sigmoid for the bulk. Full model equations and parameter tables are provided in Table S1 (Supporting Information). Figure 3c shows the measured intensity spectra via ellipsometry, where a distinct extinction coefficient peak at λ = 434 nm correspond to a phase of bi-layer quasi-2D perovskite crystals (N = 2).[25,26] In contrary, a photoluminescence peak appears at λ = 500nm which represents the bulk perovskite characteristics. Figure 3d,e shows the measured FIM results and their corresponding fits for perovskite films at λ = 437 nm and λ = 500 nm, respectively. Optical constants (n_o and n_e) required for fitting the FIM results are obtained via birefringent optical model, enabling the extraction of TDM orientation. At λ = 437 nm, the result shows n_o = 2.06, n_e = 1.57, and θ_{hor} = 0.74 while at λ = 500 nm, n_o = 2.04, n_e = 1.71, and θ_{hor} = 0.66 is obtained. The fitted n_o shows marginal increase, whereas the n_o increases significantly as the spectrum shifts from N = 2 to bulk. This is consistent with a growth of out-of-plane oscillator strength as the probe wavelength approaches the excitonic resonance of bulk-like perovsike which raises k_e, causing an increase in n_0. In contrast n_o remains comparatively flat, and the significantly larger k_o in quasi-2D films further emphasizes the relatively smaller k_e in 2D structures compared to bulk materials where $k_o \approx k_e$.[27,28] As a result, the θ_{hor} decreases from 0.74 to 0.66, indicating a shift from predominantly in-plane to mixed random emission as bulk-like domains become spectrally dominant.

At $\lambda = 465$ nm ($N = 3$), the measurement yields result that significantly deviates from those observed at $N = 2$. In this spectral region, the contribution from bulk emission is sufficiently strong that it overwhelms the structured dipole signal, resulting in an orientation distribution that trends toward random TDM, closely resembling the isotropic nature of the bulk. As a consequence, the inferred dipole orientation lacks physical credibility. This outcome illustrates a limit of the technique, implying loss of reliable interpretation when spectral overlap is significant enough to

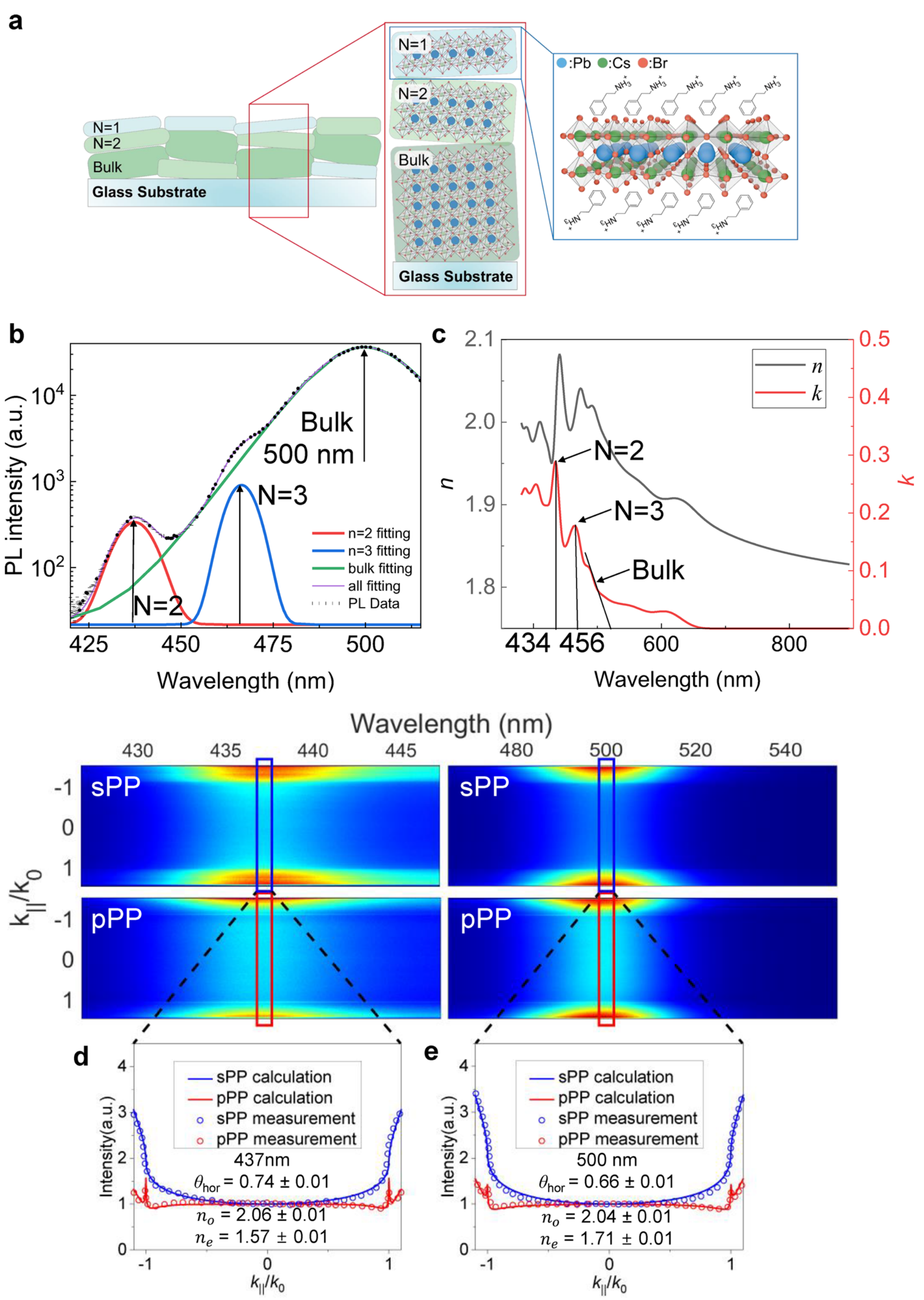

Figure 3. a) The structure of organic Halide perovskite film. b) Photoluminescence (PL) spectrum of the spin-coated quasi-2D organic Halide perovskite thin film incorporating PEABr ligands. The PL profile is deconvoluted into three distinct emission components corresponding to layered perovskite phases characterized by distinct numbers of perovskite layers (N = 2, 3, bulk) c) Refractive index and extinction coefficient of perovskite film measured via ellipsometry. Measured Spectrum resolved FIM image and intensity profiles at specific wavelengths (data points) in sPP (blue) and pPP (red) along with calculated fits (solid lines) of organic Halide perovskite film at d) 437 nm, and at e) 500 nm. [Correction added on October 23, 2025, after first online publication: figure 3 has been updated in this version.]

obscure the intrinsic signal. The fit results and retrieved parameters at $\lambda = 465$ nm are provided in Supplementary Information (see Figure S3, Supporting Information).

Ellipsometry infers thin-film optical constants via measured amplitude ratio (Ψ) and phase shift (Δ) of the reflected p- and s-polarized light. These constants arise from the difference between the Fresnel reflection of the two polarized light at the interface (R_p and R_s). In an anisotropic thin film, only the p-polarized beam contains an electric field component normal to the substrate plane (pPP$_{ver}$ in Figure 1c) and thus carries information of n_e . However, when the film thickness is much thinner than the wavelength of incident light, in the scale of tens of nanometers, accumulated phase delay during the round-trip within the layer drops, causing the n_e sensitivity to reduce to the instrument's noise floor. Thus, under these conditions, ellipsometric fitting precision is highly correlated to the product n_e and film thickness. As a result, a small difference in n_e can be compensated by a proportional change in film thickness, markedly degrading the uniqueness of the n_e solution . To address these challenges, variable-angle spectroscopic ellipsometry (VASE) acquires spectroscopic Ψ and Δ signals at multiple incidence angles, generating independent spectral datasets for each angle. These multi-angle datasets provide additional information in the optical model fitting process, enhancing the robustness and reliability of the extracted refractive index parameters. Nevertheless, as the number of incidence angles and thus data points increases, the total measurement time increases accordingly, making it impractical to obtain an unlimited dataset. Consequently, accurately extracting both n_o and n_e from a single ellipsometry data set remains challenging. This issue becomes particularly critical in quasi-2D perovskite thin films (Figure 3b), where a thickness of only a few nanometers is combined with a pronounced vertical compositional gradient originating from bulk-like domains.

FIM circumvents these limitations by performing an optical Fourier transform and recording the photoluminescence in momentum space: a single acquisition yields intensity data for numerous polar and azimuthal angles as shown in right hand side of Figure 1b. Each detection angle corresponds to a distinct optical path through the film, and the phase accumulated along that path depends on n_e. Consequently, the Fourier-plane image provides significantly increased number of orthogonal information, where each angular path serves as an independent fitting condition for refractive index extraction. Splitting the emission into sPP and pPP further decouples the ordinary and extraordinary responses, allowing n_o to be fixed by the pattern of sPP while n_e is fitted to the pattern of pPP. Moreover, because FIM analyses internally generated emission rather than reflected light, its retrieval of n_o and n_e is largely immune to the diffuse-scattering artefacts that surface roughness introduces into ellipsometric measurements. Also, the measurement is robust to the film absorption. Error analysis in Figure S4 (Supporting Information) shows that even after introducing realistic absorption ($\kappa \approx 0.118$), the peak intensities shift by < 5%, well within the fitting uncertainty, confirming that the method remains a powerful tool for extracting dipole orientation and refractive indices. FIM therefore delivers precise optical-anisotropy measurements even in ultrathin and morphologically non-uniform films where ellipsometry is fundamentally resolution-limited.

The FIM measurements in Figure 3 provide insights into the orientation of the TDMs in quai-2D perovskite films. As shown in Figure 3a and 3b, the film demonstrates a mixed phase of various number of perovskite layers from $N = 2$ to the bulk. The emergence of dominant bulk perovskite PL peak at 500 nm compared to the weak $N = 2$ emission peak at $\lambda = 437$ nm demonstrates efficient Förster resonance energy transfer (FRET) causing an energy-funneling process.[29] The TDM orientation at $\lambda = 437$ nm shows $\theta_{\text{hor}} = 0.74$, confirming a dominant horizontal oriented TDM orientation due to a significant quantum confinement effect. However, at the bulk emission $\lambda = 500$ nm, θ_{hor} decrease to 0.66 as shown in Figure 3d. The random TDM orientation at the dominant PL peak at $\lambda = 500$ nm is far from an ideal horizontal alignment that is necessary for efficient outcoupling. This result necessitates a strict design rule to avoid bulk domain emission when aiming for emissive layers with highly efficient outcoupling. Altogether, these findings highlight the unique utility of FIM in simultaneously resolving optical anisotropy and transition dipole moment orientation for ultrathin films with birefringence.

2.4. Transition Dipole Moment Orientation of Quantum Dot Films

Figure 4 shows the measured and calculated FIM polar plots as well as the surface texture of the QD film. As shown in Figure 4a, the QD heterostructure comprises CdSe/CdZnSe/ZnSeS/ZnS/oleic acid ligands with an overall size of 14 nm.[30] As shown in Figure 4b, quantum dot (QD) films exhibit rough surfaces with random voids and a root mean square roughness of $R_q = 3.4$ nm, which induces light scattering and thereby limit the precision of ellipsometry (see Figure S5, Supporting Information). Figure 4c,d shows the measured and calculated Fourier plane images with its intensity spectrum in sPP and pPP that results in the refractive index of 1.71 ± 0.01 and θ_{hor} 0.79 ± 0.01, indicating a horizontal orientation. In contrast, method utilizing FIM measures the TDM orientation and refractive index of the film simultaneously with high accuracy as shown in Figure 4d.

While the QD core has a refractive index of 2.7, the shell and ligand show lower refractive index, thus reducing the average refractive index to approximately 2.4.[31] When forming a film, voids are created within the film, reducing the refractive index even further. Consequently, the fill factor that indicates the volume proportion of QD particles within the overall film, can be determined via film's refractive index. The fill factor is shown to be 53%, with the measured refractive index of the QD film as $n = 1.71 \pm 0.01$, and assuming the refractive index of the voids to be $n = 1$.[31,32] The TDM distribution within the spin-coated QD film is horizontal to a certain degree, with θ_{hor} around 0.79 ± 0.01 as shown in Figure S6 (Supporting Information). This horizontally oriented TDM is basically due to asymmetric strain induced by lattice mismatch in the QD heterostructure and the wurtzite (WZ) crystalline phase in the QD core, which facilitates preferential orientation of crystallographic axis and strong static dipole of each QD particle. The dipole further causes highly ordered self-assembly in the QD film, leading to significant horizontal TDM orientation as confirmed from a previous study.[33]

As such, the presence of voids and the heterogeneous refractive index distribution within CdSe-based QD films complicates conventional ellipsometry measurements; however, FIM has been confirmed as a reliable alternative capable of simultaneously and accurately measuring the equivalent refractive index of the thin film and the transition dipole moment orientation under such conditions.

2.5. Accuracy and Reliability

Measurement accuracy is determined by comparing the measured refractive indices of organic thin films via FIM to the

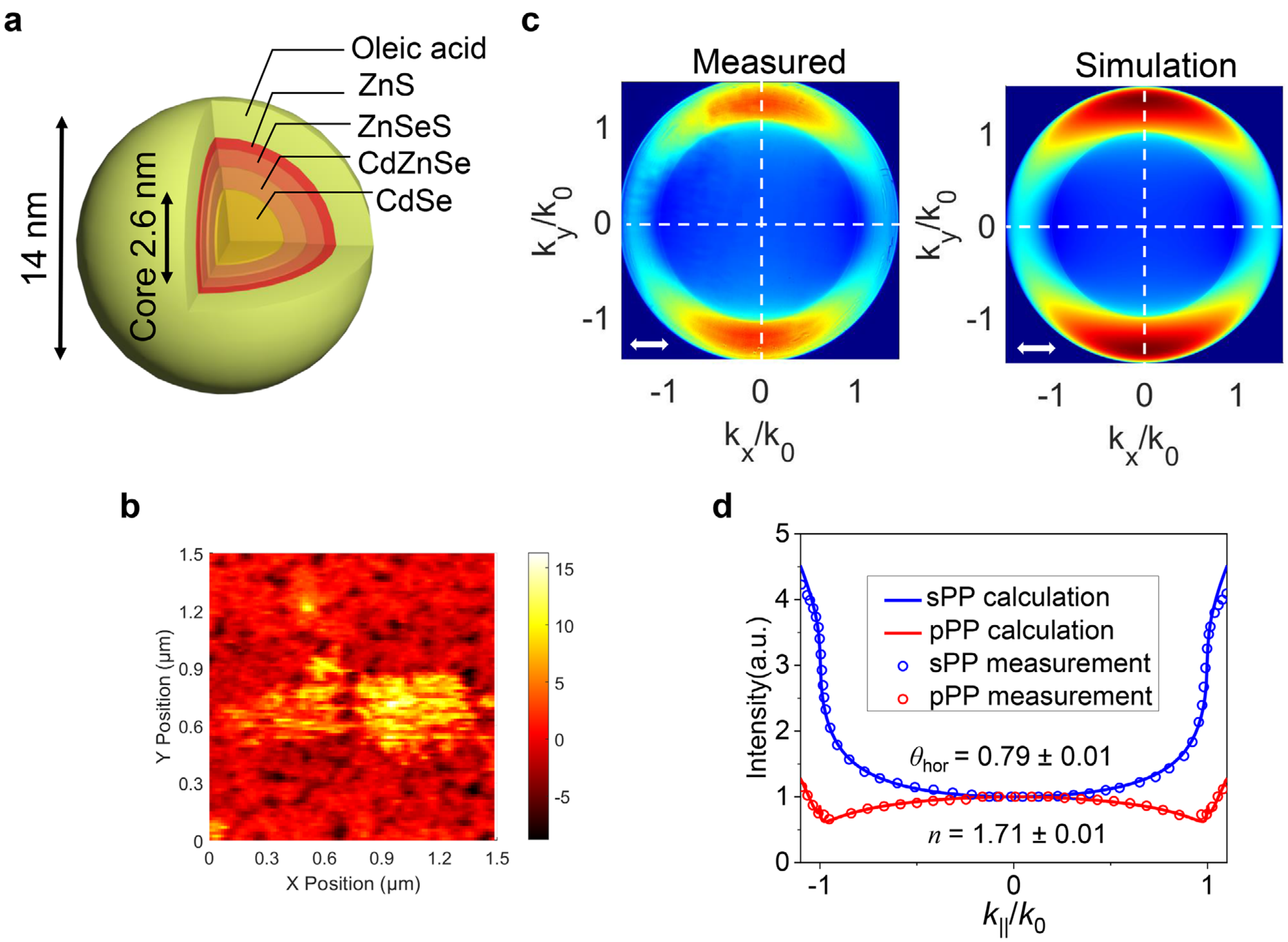

Figure 4. a) A schematic illustration showing the structure of a quantum dot. b) Surface scan of the QD film measured by atomic force microscope. c) Measured (left) and simulated (right) *k*-space polar plots via FIM. d) Measured intensity profiles of CdSe QD film (data points) in the sPP (blue) and pPP (red) along with the simulated fits (solid lines).

measurements obtained from ellipsometry, as shown in Figure S7 and Table S2 (Supporting Information). The values acquired from the two techniques are in close agreement, supporting the validity of the fitting procedure with FIM. In addition, the reliability of the measurement is evaluated by repeating the experiment 100 times at identical location on the same sample. As shown in Figure S8 (Supporting Information), both the refractive index and the θ_{hor} values varies within ±1%, indicating that the measurements are stable and reproducible. The consistency with ellipsometry and the narrow distribution of repeated measurements demonstrate that FIM provides accurate and reliable extraction of refractive indices and TDM orientations.

3. Conclusion

In this work, we present a simple and precise method for simultaneously observing the refractive index and orientation of the transition dipole moment (TDM) within a thin emissive film. Our method is particularly effective for films with rough surfaces, such as QD thin films, which are typically challenging for conventional ellipsometry. Especially, it enables accurate determination of anisotropic refractive indices, even in ultrathin birefringent films where such measurements are typically challenging. The strength of these measurements is the fact that it can extract TDM orientation and refractive index simultaneously in a single acquisition, which makes it especially effective in analyzing TDM of weakly emissive samples with critical emission decay. Using Fourier imaging microscopy, we successfully applied this technique to a variety of emissive materials, including organic phosphorescent emitters, neat molecular films, and inorganic emitters such as QDs and perovskite films. This capability offers a powerful diagnostic tool for optical characterization of emissive layers, ultimately enabling detailed nanoscale analysis that supports the advancement of advanced optoelectronic technologies.

4. Experimental Section

Sample Fabrication: Organic films were deposited on clean glass substrates via thermal evaporation. Films of mCBP (30 nm) doped with 10 vol.% emitters ($Ir(ppy)_3$, $Ir(ppy)_2(acac)$, $Ir(mphmq)_2(tmd)$) were prepared. Additional organic materials such as Alq_3 and Trz-CzCz were deposited under identical conditions. PTCDA film with a thickness of 50 nm was also thermally evaporated.

Perovskite films were prepared by spin-coating precursor solutions onto substrates. The precursor solution was prepared by dissolving 0.2 mmol each of CsBr and $PbBr_2$ in DMSO, followed by the addition of varying amounts of PEABr to achieve a molar ratio corresponding to 100% PEABr (i. e., $M_{PEABr} = M_{CsPbBr_3} = 100\%$). The solution was stirred at 80 °C for 2 h to ensure complete dissolution and homogeneity. Spin-coating was performed using a two-step procedure at 3000 rpm for 55 s, followed by thermal annealing at 100 °C for 1 minute to promote crystallization.[34]

Quantum dot (QD) films were prepared by spin-coating 20 µL of continuously graded-QD solution (20 mg mL^{-1} in Toluene) onto substrates at 2000 rpm for 30 s, yielding a final film thickness of approximately 51nm. The preparation of the cg-QD solutions was done by following the established protocols as previously reported.[30]

Fourier Imaging Microscope Measurement: The Fourier imaging microscope (FIM) comprises two integrated components: (i) an inverted photoluminescence microscope comprising a 405-nm laser and an inverted microscope (Olympus IX81) and (ii) a Fourier optical system comprising a relay lens (Thorlabs), optical filters, a linear polarizer, and a spectrometer with a 1024 × 1024 charge-coupled device (CCD) array (Princeton Instruments). Photoluminescence from the sample was collected via a ×100 oil immersion objective (NA = 1.45, Olympus). The Fourier plane was reconstructed on the CCD plane by a $f = 300$ mm relay lens. To eliminate laser reflections from the detection path, a 450 nm long-pass filter and a neutral density filter were employed. Polarization-dependent measurements were enabled by a linear polarizer, which separates orthogonal emission components corresponding to the sPP and pPP modes.

Due to the broad full-width at half-maximum of the emission spectra, which hinders unambiguous determination of the transition dipole moment orientation at a single wavelength, spectral partitioning was employed to isolate the *k*-space intensity distribution at the target wavelength. In our spectrally resolved FIM system, a linear polarizer selectively filters the s- or p-polarized emission, nd then dispersed through a slit and diffraction grating to produce a comprehensive wavelength–momentum (λ–k) maps. This enables precise extraction of *k*-space intensity profiles at specific wavelengths, enhancing the measurement accuracy of the TDM orientation.

Calculation and Fitting: The intensity spectrum on sPP solely depends on the film thickness and n_o, remaining unaffected by the n_o and the TDM orientation. Film thicknesses were measured by atomic force microscope, and n_o is determined by comparing the measured sPP spectra with calculated results based on a dyadic Green's function approach.[35] The fitting was performed over a limited *k* region, between -1.1 and 1.1 to avoid image artefacts.[3,5,36–39] The refractive index and orientation are fitted by identifying the condition that yields the minimum mean squared error (MSE) between the calculated and measured spectra. Since the calculated spectrum varies continuously with changes in the parameters, the MSE inevitably exhibits one or more local minima. Although correlations between parameters may occasionally result in multiple local minima, the set of parameters corresponding to the global minimum MSE uniquely represents the actual optical properties of the film.

Based on the obtained film thickness and n_o, the fitting strategy proceeds in two steps. First, since the influence of θ_{hor} on the pPP spectrum is stronger than that of n_o, the spectrum is fitted by varying only a single parameter, the TDM orientation ratio (θ_{hor}). Figure S9a,b (Supporting Information) demonstrate the validity of this single-parameter (θ_{hor}) fit: a contour map of the mean squared error between the measured p-polarized pattern and calculation results for different n_o and θ_{hor} values exhibits a single global minimum (marked by a circle), confirming that the fit is unique, well-converged, and independent of the initial guess.

For materials without significant birefringence ($n_e \approx n_o$), the procedure terminates at this stage. In contrast, for materials exhibiting pronounced birefringence, the same pPP spectrum is subjected to a two-parameter fitting, in which both n_o and θ_{hor} are varied simultaneously, while the thickness and n_o obtained from the sPP analysis are kept fixed. Figure S9c (Supporting Information) substantiates the adequacy of this two-parameter (n_o, θ_{hor}) fit, confirming that the fitting approach is reliable and well-converged. Using this procedure, the results obtained for various organic films are consistent with previously reported values, as summarized in Table S2 (Supporting Information).

Sample Characterization: The atomic force microscope measurements were performed using the XE-100 model from Park Systems, in non-contact mode, with a PPP-NCHR cantilever. The refractive index of the organic film was measured using the Alpha SE from J.A. Woollam Co.

Supporting Information

Supporting Information is available from the Wiley Online Library or from the author.

Acknowledgements

D.S. and S.C. contributed equally to this work. This work was supported by the Yonsei University Research Fund of 2024, Award Number 2024-22-0105, LG Display under the LGD-Yonsei Incubation Program, Award Number C2024001801, Industrial Strategic Technology Development Program (2410005219, Platform technology for enhanced OLED materials and device industry high-performance backplane and high-efficiency) funded by the Ministry of Trade, Industry & Energy (MOTIE, Korea), Global – Learning & Academic research institution for Master's·PhD students, and Postdocs(LAMP) Program of the National Research Foundation of Korea(NRF) grant funded by the Ministry of Education(No. RS-2024-00442483), and the National Research Foundation of Korea (NRF) grant funded by the Korea government (Ministry of Science and ICT) (No. RS-2025-24535263). Korea Institute for Advancement of Technology (KIAT) grant funded by the Korean Government (MOTIE) (RS-2025-02263458). [Correction added on October 22, 2025, after first online publication: The Acknowledgement section has been updated in this version.]

Conflict of Interest

The authors declare no conflict of interest.

Data Availability Statement

The data that support the findings of this study are available from the corresponding author upon reasonable request.

Keywords

anisotropic optical properties, fourierFourier imaging microscopy, nanoscale films, perovskite films, quantum dots, refractive indices, transition dipole moments

Received: June 24, 2025
Revised: August 19, 2025
Published online:

---

[1] R. Scott, J. Heckmann, A. V. Prudnikau, A. Antanovich, A. Mikhailov, N. Owschimikow, M. Artemyev, J. I. Climente, U. Woggon, N. B. Grosse, A. W. Achtstein, *Nat. Nanotechnol.* **2017**, *12*, 1155.
[2] Y. Gao, M. C. Weidman, W. A. Tisdale, *Nano Lett.* **2017**, *17*, 3837.
[3] J. A. Schuller, S. Karaveli, T. Schiros, K. He, S. Yang, I. Kymissis, J. Shan, R. Zia, *Nat. Nanotechnol.* **2013**, *8*, 271.

[4] M. J. Jurow, T. Morgenstern, C. Eisler, J. Kang, E. Penzo, M. Do, M. Engelmayer, W. T. Osowiecki, Y. Bekenstein, C. Tassone, L.-W. Wang, A. P. Alivisatos, W. Brütting, Y. Liu, *Nano Lett.* **2019**, *19*, 2489.
[5] M. A. Lieb, J. M. Zavislan, L. Novotny, *J. Opt. Soc. Am. B* **2004**, *21*, 1210.
[6] S. J. Brown, R. A. Schlitz, M. L. Chabinyc, J. A. Schuller, *Phys. Rev. B* **2016**, *94*, 165105.
[7] Y. Song, R. Liu, Z. Wang, H. Xu, Y. Ma, F. Fan, O. Voznyy, J. Du, *Sci. Adv.* **2022**, *8*, abl8219.
[8] S. Cueff, L. Berguiga, H. S. Nguyen, *Nanophotonics* **2024**, *13*, 841.
[9] A. S. Backer, W. E. Moerner, *J. Phys. Chem. B* **2014**, *118*, 8313.
[10] J. Kim, H. Zhao, S. Hou, M. Khatoniar, V. Menon, S. R. Forrest, *Phys. Rev. Appl.* **2020**, *14*, 034048.
[11] S. J. Brown, R. A. DeCrescent, D. M. Nakazono, S. H. Willenson, N. A. Ran, X. Liu, G. C. Bazan, T.-Q. Nguyen, J. A. Schuller, *Nano Lett.* **2017**, *17*, 6151.
[12] A. Fieramosca, L. De Marco, M. Passoni, L. Polimeno, A. Rizzo, B. L. T. Rosa, G. Cruciani, L. Dominici, M. De Giorgi, G. Gigli, L. C. Andreani, D. Gerace, D. Ballarini, D. Sanvitto, *ACS Photonics* **2018**, *5*, 4179.
[13] D. Pommier, R. Bretel, L. E. P. López, F. Fabre, A. Mayne, E. Boer-Duchemin, G. Dujardin, G. Schull, S. Berciaud, E. L.e Moal, *Phys. Rev. Lett.* **2019**, *123*, 027402.
[14] T. H. Taminiau, S. Karaveli, N. F. van Hulst, R. Zia, *Nat. Commun.* **2012**, *3*, 979.
[15] J. Kim, S. Hou, H. Zhao, S. R. Forrest, *Nano Lett.* **2020**, *20*, 8290.
[16] J. Kim, S. Zhang, S. Hou, B. Lee, G. Wei, S. R. Forrest, *ACS Photonics* **2021**, *8*, 1152.
[17] N. Danz, A. Occhicone, C. Pflumm, P. Munzert, F. Michelotti, D. Michaelis, *Opt. Express* **2021**, *29*, 6608.
[18] H. Zhao, J. Kim, K. Ding, M. Jung, Y. Li, H. Ade, J. Y. Lee, S. R. Forrest, *Adv. Mater.* **2023**, *35*, 2210794.
[19] R. A. DeCrescent, N. R. Venkatesan, C. J. Dahlman, R. M. Kennard, M. L. Chabinyc, J. A. Schuller, *ACS Nano* **2019**, *13*, 10745.
[20] L. Maserati, S. Refaely-Abramson, C. Kastl, C. T. Chen, N. J. Borys, C. N. Eisler, M. S. Collins, T. E. Smidt, E. S. Barnard, M. Strasbourg, E. A. Schriber, B. Shevitski, K. Yao, J. Nathan Hohman, P. J. Schuck, S. Aloni, J. B. Neaton, A. M. Schwartzberg, **2021**, https://doi.org/10.1039/C9MH01917K.
[21] M. Brotons-Gisbert, R. Proux, R. Picard, D. Andres-Penares, A. Branny, A. Molina-Sánchez, J. F. Sánchez-Royo, B. D. Gerardot, *Nat. Commun.* **2019**, *10*, 3913.
[22] L. Sigl, M. Troue, M. Katzer, M. Selig, F. Sigger, J. Kiemle, M. Brotons-Gisbert, K. Watanabe, T. Taniguchi, B. D. Gerardot, A. Knorr, U. Wurstbauer, A. W. Holleitner, *Phys. Rev. B* **2022**, *105*, 035417.
[23] B. Russ, T.-T. Lin, H. Elenteny, C. N. Eisler, *ACS Photonics* **2025**, 3217, https://doi.org/10.1021/acsphotonics.5c00684.
[24] J. A. Ekhoff, K. L. Rowlen, *Anal. Chem.* **2002**, *74*, 5954.
[25] Y. Gao, Y. Liu, F. Zhang, X. Bao, Z. Xu, X. Bai, M. Lu, Y. Wu, Z. Wu, Y. Zhang, Q. Wang, X. Gao, Y. Wang, Z. Shi, J. Hu, W. W. Yu, Y. Zhang, *Adv. Mater.* **2022**, *34*, 2207445.
[26] W. Bi, Q. Cui, P. Jia, X. Huang, Y. Zhong, D. Wu, Y. Tang, S. Shen, Y. Hu, Z. Lou, F. Teng, X. Liu, Y. Hou, *ACS Appl. Mater. Interfaces* **2020**, *12*, 1721.
[27] G. Mannino, I. Deretzis, E. Smecca, A. La Magna, A. Alberti, D. Ceratti, D. Cahen, *J. Phys. Chem. Lett.* **2020**, *11*, 2490.
[28] M. Steger, S. M. Janke, P. C. Sercel, B. W. Larson, H. Lu, X. Qin, V. W. Yu, V. Blum, J. L. Blackburn, *Nanoscale* **2022**, *14*, 752.
[29] L. Zhang, C. Sun, T. He, Y. Jiang, J. Wei, Y. Huang, M. Yuan, *Light Sci. Appl.* **2021**, *10*, 61.
[30] J. Lim, Y.-S. Park, V. I. Klimov, *Nat. Mater.* **2018**, *17*, 42.
[31] D. B. Dement, M. Puri, V. E. Ferry, *J. Phys. Chem. C* **2018**, *122*, 21557.
[32] D. a. G. Bruggeman, *Ann. Phys.* **1935**, *416*, 636.
[33] H. Xu, J. Song, P. Zhou, Y. Song, J. Xu, H. Shen, S. Fang, Y. Gao, Z. Zuo, J. M. Pina, O. Voznyy, C. Yang, Y. Hu, J. Li, J. Du, E. H. Sargent, F. Fan, *Nat. Photonics* **2024**, *18*, 186.
[34] M. Ban, Y. Zou, J. P. H. Rivett, Y. Yang, T. H. Thomas, Y. Tan, T. Song, X. Gao, D. Credgington, F. Deschler, H. Sirringhaus, B. Sun, *Nat. Commun.* **2018**, *9*, 3892.
[35] K. Celebi, T. D. Heidel, M. A. Baldo, *Opt. Express* **2007**, *15*, 1762.
[36] P. Liehm, C. Murawski, M. Furno, B. Lüssem, K. Leo, M. C. Gather, *Appl. Phys. Lett.* **2012**, *101*, 253304.
[37] J. A. Kurvits, M. Jiang, R. Zia, *J. Opt. Soc. Am. A* **2015**, *32*, 2082.
[38] T. H. Taminiau, F. D. Stefani, F. B. Segerink, N. F. van Hulst, *Nature Photonics* **2008**, *2*, 234.
[39] M. Böhmler, N. Hartmann, C. Georgi, F. Hennrich, A. A. Green, M. C. Hersam, A. Hartschuh, *Opt. Express* **2010**, *18*, 16443.